

Systematic Features of Axi-Symmetric Neutrino-Driven Core-Collapse Supernova Models in Multiple Progenitors

KO NAKAMURA

*Faculty of Science and Engineering, Waseda University, Ohkubo 3-4-1, Shinjuku, Tokyo 169-8555
nakamura.ko@heap.phys.waseda.ac.jp*

Tomoya TAKIWAKI *

Center for Computational Astrophysics, National Astronomical Observatory of Japan, 2-21-1 Osawa, Mitaka, Tokyo 181-8588

Takami KURODA

*Department of Physics, University of Basel, Klingelbergstrasse 82, 4056 Basel, Switzerland
and*

Kei KOTAKE

Department of applied physics, Fukuoka University, 8-19-1 Nanakuma Jonan, Fukuoka 814-0180

(Received 2015 February 12; accepted 2015 July 24)

Abstract

We present an overview of two-dimensional (2D) core-collapse supernova simulations employing neutrino transport scheme by the isotropic diffusion source approximation. We study 101 solar-metallicity, 247 ultra metal-poor, and 30 zero-metal progenitors covering zero-age main sequence mass from $10.8 M_{\odot}$ to $75.0 M_{\odot}$. Using the 378 progenitors in total, we systematically investigate how the differences in the structures of these multiple progenitors impact the hydrodynamics evolution. By following a long-term evolution over 1.0 s after bounce, most of the computed models exhibit neutrino-driven revival of the stalled bounce shock at $\sim 200 - 800$ ms postbounce, leading to the possibility of explosion. Pushing the boundaries of expectations in previous one-dimensional (1D) studies, our results confirm that the compactness parameter ξ that characterizes the structure of the progenitors is also a key in 2D to diagnose the properties of neutrino-driven explosions. Models with high ξ undergo high ram pressure from the accreting matter onto the stalled shock, which affects the subsequent evolution of the shock expansion and the mass of the protoneutron star under the influence of neutrino-driven convection and the standing accretion-shock instability. We show that the accretion luminosity becomes higher for models with high ξ , which makes the growth rate of the diagnostic explosion energy higher and the synthesized nickel mass bigger. We find that these explosion characteristics tend to show a monotonic increase as a function of the compactness parameter ξ .

Key words: Hydrodynamics—Neutrinos—Nuclear reactions, nucleosynthesis, abundances—Supernovae: general

1. Introduction

The explosability of massive stars depends sensitively on the presupernova structures (e.g., O'Connor & Ott 2011; Ugliano et al. 2012; Couch & Ott 2013; Sukhbold & Woosley 2014). For low-mass progenitors with O-Ne-Mg core, the neutrino mechanism works successfully to explode in one-dimensional (1D) simulations because of the tenuous envelope (Kitaura et al. 2006). For more massive progenitors with iron core, multi-dimensional (multi-D) effects such as neutrino-driven convection (e.g., Bethe 1990; Herant et al. 1994; Burrows et al. 1995; Janka & Müller 1996; Müller & Janka 1997) and the standing-accretion-shock-instability (SASI, Blondin et al. 2003; Foglizzo et al. 2006; Foglizzo et al. 2007; Ohnishi et al. 2006; Blondin & Mezzacappa 2007; Iwakami et al. 2008; Iwakami et al. 2009; Fernández & Thompson 2009; Guilet & Foglizzo 2012; Hanke et al. 2012; Foglizzo et al.

2012; Couch 2013; Fernández et al. 2014, see Foglizzo et al. 2015 for a review) have been suggested to help the onset of the neutrino-driven explosion. Recently this has been confirmed by a number of self-consistent two-(2D) and three-dimensional (3D) simulations (e.g., Buras et al. 2006; Ott et al. 2008; Marek & Janka 2009; Bruenn et al. 2013; Suwa et al. 2010; Suwa et al. 2014; Müller et al. 2012a; Müller et al. 2013; Takiwaki et al. 2012; Takiwaki et al. 2014; Hanke et al. 2013; Dolence et al. 2014; Bruenn et al. 2014; Müller & Janka 2014, see Mezzacappa et al. 2015; Janka 2012; Burrows 2013; Kotake et al. 2012 for recent review)). Up to now, the number of these state-of-the-art models amounts to ~ 40 covering the zero-age main sequence (ZAMS) mass from $8.1 M_{\odot}$ (Müller et al. 2012a) to $27 M_{\odot}$ (Hanke et al. 2013).

Based on stellar evolutionary calculations, on the other hand, *hundreds* of CCSN progenitors are available now, depending on a wide variety of the ZAMS mass, metallicity, rotation, and magnetic fields (e.g., Nomoto & Hashimoto 1988; Woosley & Weaver 1995; Woosley et al. 2002; Woosley & Heger 2007; Heger et al. 2000; Heger

* Present Address is RIKEN, 2-1 Hirosawa, Wako, Saitama 351-0198

et al. 2005; Limongi & Chieffi 2006). These huge sets of CCSN progenitors, aided as well as by development of high-performance computers and numerical schemes, make *systematic* numerical study of CCSNe possible.

By performing general-relativistic (GR) 1.5D simulations for over 100 presupernova models using a leakage scheme, O'Connor & Ott (2011) were the first to point out that the postbounce dynamics and the progenitor-remnant connections are predictable basically by a single parameter, compactness of the stellar core at bounce (see also O'Connor & Ott 2013). Along this line, Ugliano et al. (2012) performed 1D hydrodynamic simulations for 101 progenitors of Woosley et al. (2002). By replacing the proto-neutron star (PNS) interior with an inner boundary condition, they followed an unprecedentedly long-term evolution over hours to days after bounce in spherical symmetry. Their results also lent support to the finding by O'Connor & Ott (2011) that the compactness parameter is a good measure to diagnose the progenitor-explosion and the progenitor-remnant correlation (see also Pejcha & Thompson 2014; Perego et al. 2015).

Joining in these efforts but going beyond the previous 1D approach, we perform neutrino-radiation hydrodynamics simulations in two dimensions using the whole presupernova series (101 solar-metallicity models, 247 ultra metal-poor models, and 30 zero-metal models) of Woosley et al. (2002). Without the excision inside the PNS, we can self-consistently follow a long-term evolution starting from the onset of core-collapse, bounce, neutrino-driven shock-revival, until the revived shock comes out of the iron core. The goal of our 2D models is not to determine the very final fate of a massive star (which requires 3D-GR models with detailed transport scheme (e.g., Kuroda et al. 2015)), but to study the systematic dependence of the progenitors' structure on the shock revival time, diagnostic explosion energy, mass of remnant object, and nucleosynthetic yields. To this end, this study is the first attempt in the multi-D context.

Section 2 describes the numerical setup, including explanation of our numerical scheme (Section 2.1), structure of the solar-metallicity 101 progenitors (Section 2.2), and discussion on effects of our choice of the outer boundary (Section 2.3). Results start from Section 3 where we first focus on the hydrodynamics evolution of the 101 solar-metallicity progenitors, and then move on to analyze the results in terms of the compactness parameters (Section 4). Section 5 presents results of the 247 ultra-metal-poor and the 30 zero-metal progenitors. We summarize our results and discuss their implications in Section 6.

2. Numerical setup

2.1. Numerical scheme

The employed numerical methods are based on those in Takiwaki et al. (2014). Our 2D models are computed on a spherical polar grid of 384 non-equidistant radial zones from the center up to 5000 km. Our spatial grid has a finest mesh spacing $dr_{\min} = 0.5$ km at the center and dr/r is better than 1.8 % at $r > 100$ km. Our hydrodynamic

scheme requires two ghost cell layers just above the outer boundary. We fix the density and velocity in the ghost cells to be the values there of the progenitor models (see section 2.3 for the effects of the outer boundary). We set 128 equidistant angular zones covering $0 \leq \theta \leq \pi$ so that the angular resolution is 1.4° . We employ the equation of state (EOS) by Lattimer & Swesty (1991) with a compressibility modulus of $K = 220$ MeV (LS220). For the calculations presented here, self-gravity is computed by a Newtonian monopole approximation and our code is updated, from the ZEUS-MP (Hayes et al. 2006) code as was used in Takiwaki et al. (2014), to use high-resolution shock capturing scheme with an approximate Riemann solver ofinfeldt (1988). As described in Nakamura et al. (2014), we take into account explosive nucleosynthesis and the energy feedback into hydrodynamics by solving a 13 α -nuclei network including ^4He , ^{12}C , ^{16}O , ^{20}Ne , ^{24}Mg , ^{28}Si , ^{32}S , ^{36}Ar , ^{40}Ca , ^{44}Ti , ^{48}Cr , ^{52}Fe , and ^{56}Ni . The nuclear energy compensates for energy loss via endothermic decomposition of iron-like NSE nuclei to lighter elements (see Appendix of Nakamura et al. (2014) for more details).

To solve spectral transport of electron- (ν_e) and anti-electron neutrinos ($\bar{\nu}_e$), we employ the isotropic diffusion source approximation (IDSA, Liebendörfer et al. 2009). We take a ray-by-ray approach, in which the neutrino transport is solved along a given radial ray assuming that the hydrodynamic medium for the direction is spherically symmetric (e.g., Buras et al. 2006). Although one needs to deal with the lateral transport more appropriately (e.g., Sumiyoshi et al. 2014; Dolence et al. 2014), this approximation is useful because of the high computational efficiency in parallelization, which allows us to explore the more systematic progenitor survey based on the radiation-hydrodynamics models than ever in this study. Regarding heavy-lepton neutrinos ($\nu_x = \nu_\mu, \nu_\tau, \bar{\nu}_\mu, \bar{\nu}_\tau$), we employ a leakage scheme to include the ν_x cooling via pair, photo and plasma processes (see Takiwaki et al. 2014 for more details). To induce non-spherical instability, we add initial seed perturbations by zone-to-zone random density variations with an amplitude less than 1%.

There is still a debate about whether explosions are obtained more easily in low-resolution simulations than in high-resolution ones and how much resolutions are needed to obtain a convergence (e.g., Radice et al. (2015)). In Appendix 1, we discuss the resolution dependence of our 2D results.

2.2. Progenitor models

The investigated solar-metallicity progenitors with iron cores (Woosley et al. 2002) are given in 0.2 M_\odot steps between 10.8 M_\odot (s10.8) and 28.2 M_\odot (s28.2), further from 29 M_\odot (s29) up to 40 M_\odot (s40) in 1.0 M_\odot steps, and a 75 M_\odot model (s75), 101 progenitors in total. The structure of these stars, such as the density profiles and the pre-collapse mass distributions has been already described in Ugliano et al. (2012). Here for convenience, we show the mass distribution of some selected models at a pre-collapse stage and the time of core bounce (Figure 1). Before bounce, the distribution varies from models to

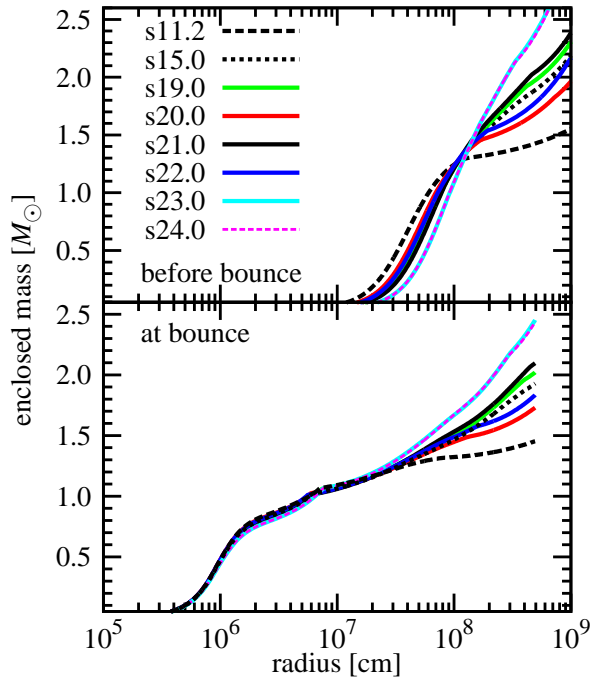


Fig. 1. Mass distribution of some selected models at a pre-collapse stage (top panel) and at the time of core bounce (bottom).

models, especially at the outer radius. The mass distribution of the collapsing core dynamically changes after the onset of collapse, but at bounce, the mass distributions remain almost identical within $\sim 2 \times 10^7$ cm among the different progenitor models (bottom panel).

To characterize the progenitor structures, we estimate the compactness parameter ξ following O’Connor & Ott (2011) as the ratio of mass M and the enclosed radius $R(M)$,

$$\xi_M \equiv \frac{M/M_\odot}{R(M)/1000\text{km}}. \quad (1)$$

The previous studies used $M = 2.5 M_\odot$ (O’Connor & Ott 2011; Ugliano et al. 2012) or $1.75 M_\odot$ (O’Connor & Ott 2013) and estimated ξ_M at the time of core bounce. On the other hand, the outer radius of our computational domain (5000 km) is too small to contain $2.5 M_\odot$ for all models and even $1.75 M_\odot$ for some less massive models (see Figure 1). In this paper, we estimate ξ_M at $M = 2.0$ and $2.5 M_\odot$ ($\xi_M = \xi_{2.0}, \xi_{2.5}$) directly from the progenitor models. It should be noted that our definition of $\xi_{2.5}$ gives almost the same value as the compactness estimated at bounce, because the radius R enclosing $2.5 M_\odot$ is far from the center and the radial velocity v_R there is very small (e.g., for s15.0 model, $R = 1.7 \times 10^9$ cm and $v_R = -6.8 \times 10^6$ cm s $^{-1}$). By comparing the top to bottom panel of Figure 1, the position of the outer envelope ($\gtrsim 10^8$ km) changes very slightly. This is because of the long dynamical time scale there compared to the short

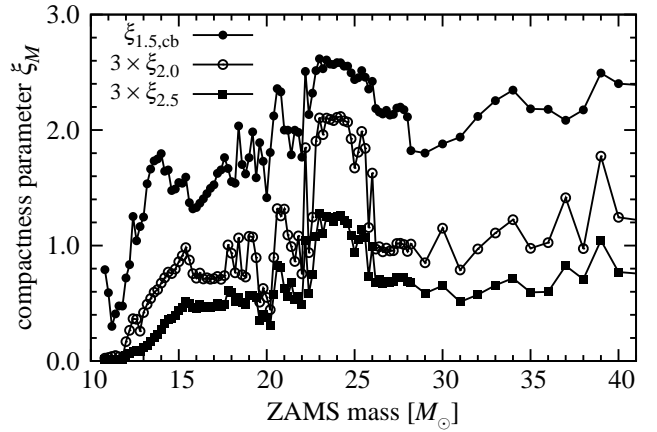


Fig. 2. Three choices of the compactness parameters ξ_M as a function of ZAMS mass. They are estimated at $M = 1.5 M_\odot$ ($\xi_{1.5,\text{cb}}$), $2.0 M_\odot$ ($\xi_{2.0}$), and $2.5 M_\odot$ ($\xi_{2.5}$) from top to bottom. Note that $\xi_{1.5,\text{cb}}$ is estimated at the time of core bounce as in the previous studies. The others are from pre-collapse data and enhanced by a factor of three for comparison. Model s75 is out of this plot but has $\xi_{1.5,\text{cb}} = 2.0$, $\xi_{2.0} = 0.17$, and $\xi_{2.5} = 0.11$.

time period before bounce (~ 200 ms). Actually $\xi_{2.5}$ of s15.0 model in our definition is 0.149, which is very close to the value (0.150) estimated by O’Connor & Ott (2011) at bounce.

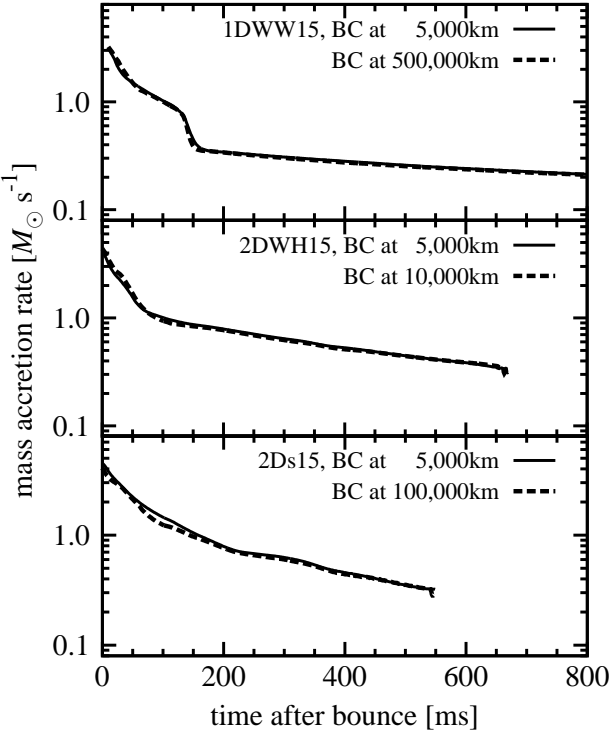
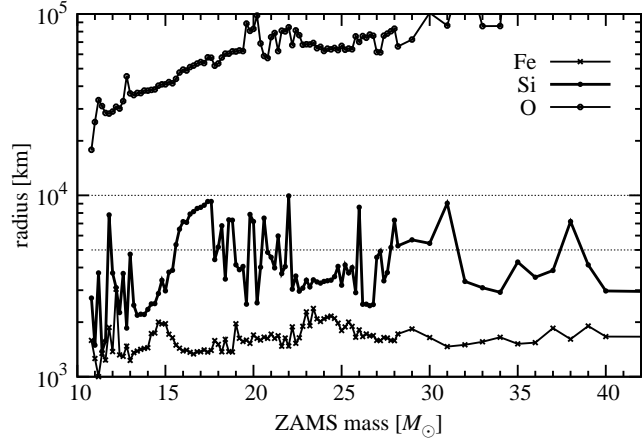
Figure 2 compares ξ_M estimated at $M = 1.5 M_\odot$ ($\xi_{1.5,\text{cb}}$), $2.0 M_\odot$ ($\xi_{2.0}$), and $2.5 M_\odot$ ($\xi_{2.5}$). Note that $\xi_{1.5,\text{cb}}$ is estimated at the time of core bounce, whereas the others are directly estimated from the progenitor data. All of these profiles show a similar trend, for example a high compactness bump in the 22 to 26 M_\odot mass range. Zigzag variations of the compact parameter can be seen for all the lines with the different choice of M , although the amplitude becomes smaller for ξ_M with larger M . Among all the 101 models, the s11.2 progenitor has the smallest value of the compactness parameter, which is easily seen for the choice of $\xi_{1.5,\text{cb}}$ (filled circles). The quantities of the compactness parameters for some representative models are listed in Table 1. It includes $\xi_{1.5}$ from the pre-collapse data and 15 M_\odot progenitors from Woosley & Weaver (1995) (WW15) and Woosley & Heger (2007) (WH15) as a reference. Metal-deficient progenitors are discussed in Section 5.

2.3. Boundary condition

Our simulation domain is limited within the radius of 5,000 km so that we can reduce computational cost and carry out 2D self-consistent simulations for the 378 progenitors. This relatively small spatial domain (5,000 km), however, might affect the hydrodynamics evolution long after bounce. To clarify this, we check the effects of the outer boundary by estimating the mass accretion rate at different radii. We focus on the mass accretion rate because it predominantly affects the explosion properties as

Table 1. Variations of the compactness parameters from the solar-metallicity progenitors (Woosley et al. 2002)

model	$\xi_{1.5,cb}$	$\xi_{1.5}$	$\xi_{2.0}$	$\xi_{2.5}$
s11.2	0.300	0.195	0.014	0.005
s15.0	1.546	0.862	0.298	0.149
s19.0	1.761	0.911	0.374	0.194
s20.0	1.414	0.671	0.187	0.127
s21.0	2.000	0.971	0.455	0.215
s22.0	1.766	0.868	0.258	0.165
s23.0	2.617	1.000	0.720	0.434
s24.0	2.583	0.998	0.721	0.427
s30	1.880	0.938	0.394	0.222
s40	2.402	0.990	0.427	0.263
s75	2.004	0.890	0.168	0.112
WW15	0.765	0.592	0.194	0.085
WH15	1.220	0.871	0.335	0.181

**Fig. 3.** Mass accretion rate of $15 M_{\odot}$ progenitor models with outer boundaries at different radii. The lines given by 2D simulations of WH15 model (middle panel), and s15 model (bottom), are truncated when the shock touches 500 km at $t_{pb} \sim 670$ ms, and ~ 550 ms, respectively. 1D simulations of WW15 model (top) do not present shock revival. The difference of the boundary position does not affect the mass accretion rate in all the chosen progenitors.**Fig. 4.** Radius of Fe core surface, Si/O interface, and top of O layer for solar-metallicity models.

we will discuss later.

In Figure 3, we show the mass accretion history of the three progenitor models with the same ZAMS mass ($15 M_{\odot}$); WW15 (Woosley & Weaver 1995) (top panel), WH15 (Woosley & Heger 2007) (middle panel), and s15 (Woosley et al. 2002) (bottom panel), respectively. Following Müller & Janka (2014), we estimate the mass accretion rate at the radius of 500 km in Figure 3. The radius of the outer boundary (R_{out}) is taken either at 5000 km or at the more distant radius 500,000 km (top panel), 10,000 km (middle panel), or 100,000 km (bottom panel), respectively. Note that the shock revival is not obtained in the WW15 model that is computed in 1D, whereas the shock revival is obtained at $t_{400} = 688$ –691 ms and 556–571 ms in the 2D simulations for the WH15 and s15 models, respectively. In the 2D models, the mass accretion rate is only shown before the shock revival (e.g., middle and bottom panels of Figure 3) because the mass accretion rate at 500 km can be affected by the non-radial motions of the expanding shock.

From Figure 3, it is shown that the mass accretion rate (before the shock reaches at the radius of 500 km) is very similar for models with the different R_{out} . It should be noted that the mass accretion rate of the WW15 model shows a sudden drop from $0.8 M_{\odot} s^{-1}$ to $0.3 M_{\odot} s^{-1}$ at $t_{pb} \sim 150$ ms (t_{pb} ; postbounce time) then gradually decreases to $0.2 M_{\odot} s^{-1}$. This is in a good agreement with the previous results using the same progenitor model (e.g., Figure 1 in Murphy & Burrows (2008) and Figure 1 in Hanke et al. (2012)). All of these facts support that our boundary conditions well imitate the density structure out of the boundary of these three $15 M_{\odot}$ models and the boundary effect is not significant for these models.

However, what if there would exist a large number of progenitors that would have shell interfaces with sharp density gradients beyond our computational domain (5000 km)? Figure 4 shows the position of the shell interfaces for all the solar-metallicity models employed in our study.

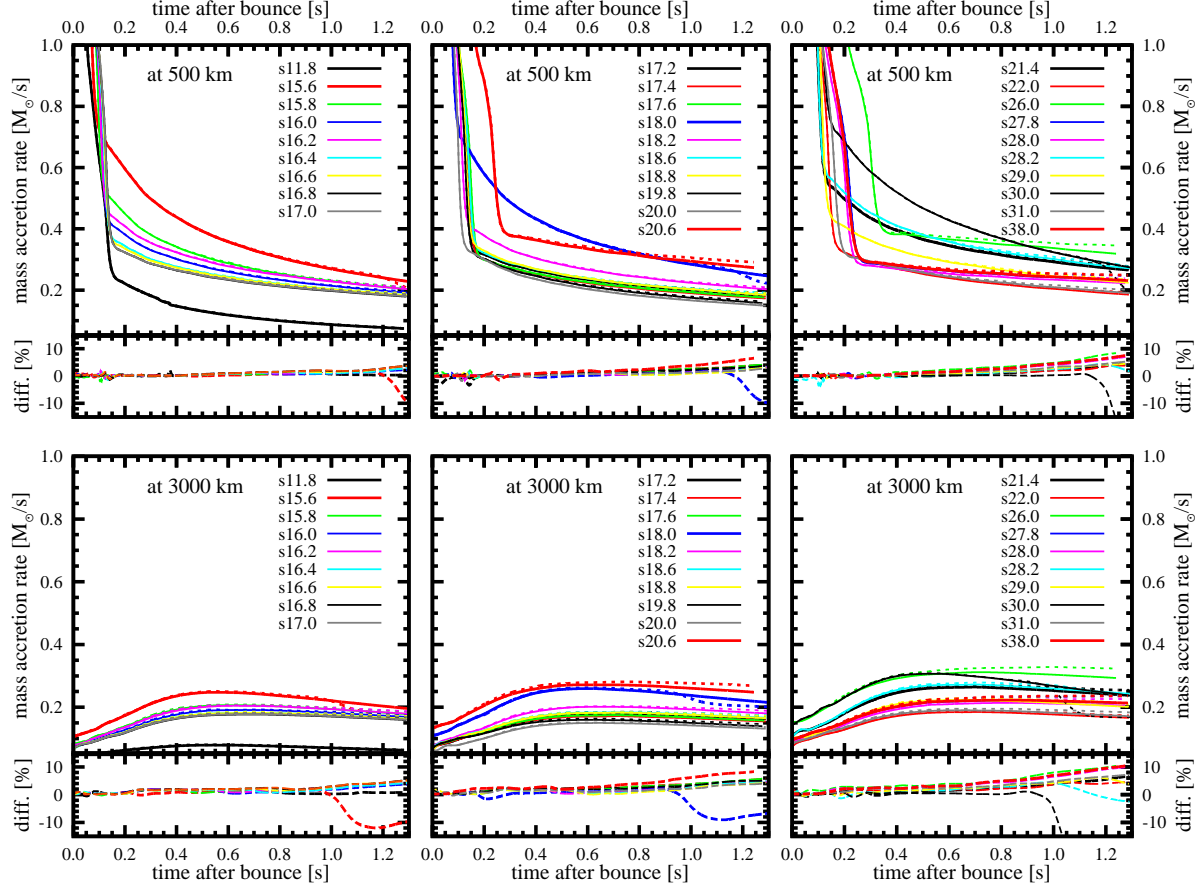


Fig. 5. Comparison of the mass accretion rate between 1D models with the outer boundary at the radius of $r = 5,000$ km (\dot{M}_5 , solid lines) and $10,000$ km (\dot{M}_{10} , dotted). Twenty-nine solar-metallicity models which have the Si/O interface between the radii of $5,000$ km and $10,000$ km are shown (see also Figure 4). Top: the mass accretion rate estimated at $r = 500$ km, representing the accretion onto a stalling shock front. Bottom: same as the top panels but estimated at $r = 3,000$ km, representing the accretion rate onto an expanding shock front in 2D models. Relative differences between the models with the two different outer boundary positions $(\dot{M}_{10} - \dot{M}_5)/\dot{M}_5$ are presented at the lower panel of each plot in percentage.

Here we define the radius of silicon (Si) layer at the position where the most abundant element changes from silicon to oxygen (O). Out of the 101 models, we identified 29 models that have the Si/O interface at the radius between $5,000$ and $10,000$ km (horizontal dotted lines). For these models having the shell interfaces above $5,000$ km, we conduct 1D simulations and plot the mass-accretion rate history in Figure 5 to examine the effects of the outer boundary positions. In each model, we vary the position of the outer boundary, either at the radius of $5,000$ km (shown by solid lines) or at $10,000$ km (dotted lines).

From each panel of Figure 5, it is shown that all of the examined models with the outer boundary at $r = 5,000$ km show very small differences (less than a few percent) from the ones with the boundary at $r = 10,000$ km before $t_{\text{pb}} \sim 0.9$ s. In this epoch, the material initially located at $r > 5,000$ km is still at $r > 3,000$ km and the boundary effect is almost negligible. After $t_{\text{pb}} \sim 0.9$ s, the material initially out of the radius of $5,000$ km begins passing through the radius of $r = 3,000$ km. Among the 29 progenitors (with shell interfaces above $5,000$ km, see also Figure 4), only 3

models show a remarkable feature in the mass accretion rate. As shown in the bottom panels of Figure 5, s15.6 (a red dotted line in the left panel), s18.0 (a blue dotted line in the middle panel), and s30.0 (a black thin-dotted line in the right panel) with the outer boundary at $r = 10,000$ km show a sudden drop ($\gtrsim 10\%$) at $t_{\text{pb}} \sim 1.0$ s, followed by the drop of the accretion rate in the top panels at $t_{\text{pb}} \sim 1.2$ s. This decrease of the accretion rate in these three models is caused by a density jump at the Si/O interface initially located at the radius $r > 5,000$ km, which cannot be taken into account by the models with the outer boundary at $r = 5,000$ km. In contrast to the models s15.6, s18.0, and s30.0, 10% level increases are observed in the models s20.6, s26.0, s28.0, and s38.0. This is because these models have a relatively high density envelope, for which our choice of the boundary position (at $5,000$ km) underestimates the mass accretion rate compared to that at $10,000$ km. There might be such models with high density envelope in the rest 72 progenitors other than the four of 29 progenitors discussed here.

To quantify the boundary effects on these models, we

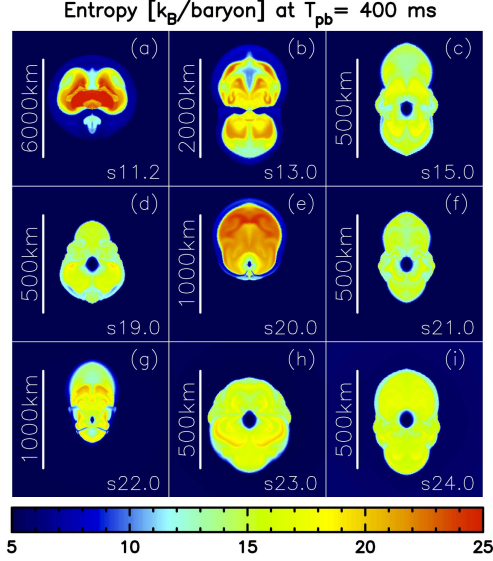


Fig. 6. Entropy distributions in unit of k_B per baryon for selected nine models at $t_{pb} = 400$ ms. Shown are models s11.2 (a) to s24.0 (i), from top-left to bottom-right. Note the different scale in each panel.

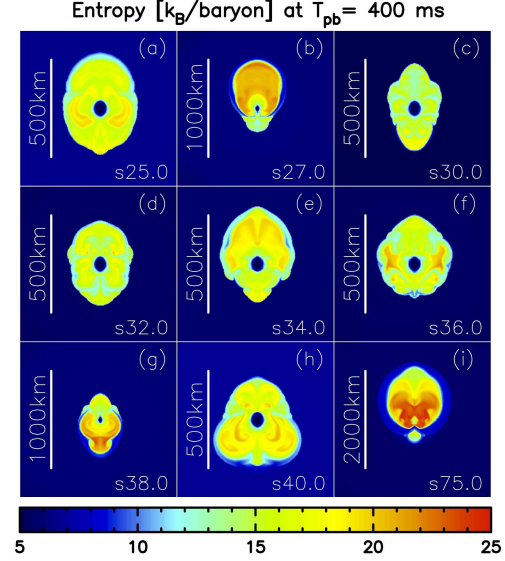


Fig. 7. Same as Figure 6 but for models s25.0 (a) to s75.0 (i), from top-left to bottom-right.

perform 2D simulations for s38.0 model in the following way. Using the same setups as our fiducial model, the density out of the maximum shock radius is manually changed when the shock reaches 3000 km. We find that increase (decrease) of the density by 10 % results in 2.8 % (0.53 %) change of the diagnostic energy and negligibly small difference of the PNS mass (< 0.03 %) at the time when the shock reaches the outer boundary at 5000 km. This is simply because of a small mass accretion rate ($< 0.3 M_\odot \text{ s}^{-1}$) at this phase and a short period until the simulations are terminated when the shock reaches the outer boundary. Thus, we conclude that the boundary effects on the mass accretion rate in the late postbounce phase is not influential to our systematic study.

3. Results

For all the solar-metallicity 101 models (and also the additional 277 models discussed in Section 5), the bounce shock stalls in a spherically symmetric manner and only after that, we observe a clear diversity of the multi-D hydrodynamics evolution in the postbounce (pb) phase. Figures 6 and 7 show a snapshot of entropy distribution for selected 18 solar-metallicity models at $t_{pb} = 400$ ms. For some less massive progenitors (e.g., model s11.2 in Figure 6(a)), the shock is reaching close to the outer boundary of the computational domain with developing pronounced unipolar and dipolar shock deformations. At this time, the shock of the most massive progenitor (s75.0 in Figure 7(i)) is reaching an average radius of $\langle r \rangle \sim 1000$ km, whereas the shock of s24.0 (in Figure 6(i)) still wobbles around at $\langle r \rangle \sim 200$ km. This demonstrates that the ZAMS mass is not a good criterion to diagnose the possibility of explosion.

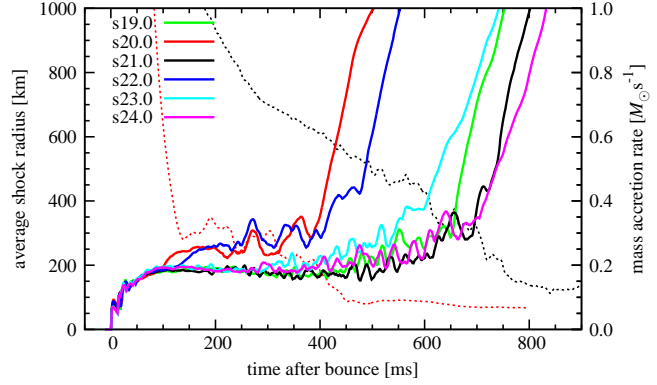


Fig. 8. Average shock radii (thick solid lines) and mass-accretion rate of the collapsing stellar core at 500 km (thin dashed lines) for some selected models.

This is more clearly visualized in Figure 8, showing time evolution of average shock radii for six models in the mass range between $19.0 M_\odot$ and $24.0 M_\odot$. The shock revival is shown to occur earlier for s20.0 (red line) and s22.0 (blue line) compared to the lighter progenitors s19.0 (green line) and s21.0 (black line). Comparing with Figure 2, it can be seen that the compactness parameter (Equation (1)) is smaller for s20.0 and s22.0 in the chosen mass range. The smaller compactness is translated into smaller mass accretion rate onto the stalled bounce shock. For model s20.0 ($\xi_{2.0} = 0.19$, red line in Figure 8), the relatively earlier shock revival (~ 100 ms post-bounce) coincides with the sharp decline of the accretion rate (dashed red line). After that, the accretion rate gradually decreases to $\sim 0.1 M_\odot \text{ s}^{-1}$ till $t_{400} = 420$ ms at this time the revived shock has expanded to an average ra-

dius of $\langle r \rangle = 400$ km. Here t_{400} is a useful measure to qualify the vigor of the shock revival (e.g., Hanke et al. 2012). On the other hand, model s21.0 has high compactness ($\xi_{2.0} = 0.46$), which leads to the high accretion rate (black dashed line in Figure 8). It takes ~ 500 ms for the sloshing shock of model s21.0 (black solid line in the Figure 8) to gradually turn into a pronounced expansion later on and 700 ms to arrive at $\langle r \rangle = 400$ km ($t_{400} = 700$ ms).

Note in Figure 8 that the correlation between the compactness and t_{400} is rather weak. In the Appendix 2, we attempt to find the alternative compactness parameter by which the correlation is slightly improved.

The gravitational mass of PNS and the *diagnostic* explosion energy¹ are also shown in Figures 9 and 10 as a function of post-bounce time. Here the PNS is defined by the region where the density $\rho > 10^{11}$ g cm⁻³. The PNS mass is almost converged in our simulation time and the value at the final simulation time $t = t_{\text{fin}}$ has a clear correlation with the compactness parameter. In fact, the PNS masses become smaller for models with smaller compactness parameter (s20.0 drawn in red line and s22.0 in blue) and bigger for models with higher compactness (s23.0 in sky blue and s24.0 in magenta) and the other two models (s19.0 in green and s21.0 in black) have the intermediate values.

In Figure 9, the horizontal dotted line represents the maximum gravitational mass ($2.04M_{\odot}$) of a cold neutron star (NS) for the LS220 EOS employed in this work. As seen, the PNS masses of our most “compact” models (e.g., s23.0 (sky blue line) and s24.0 (magenta line)) exceed the limit. Here it should be noted that the above threshold is for a cold NS, whereas the PNS soon after bounce is still hot. At this phase, the contribution of thermal pressure to the maximum mass cannot be neglected, so that the maximum mass of the hot PNS is bigger than that of the cold NS (O’Connor & Ott 2011; Hempel et al. 2012). Based on a systematic 1D GR simulation with approximate neutrino transport, O’Connor & Ott (2011) showed that the maximum gravitational mass of the hot PNSs, which is bigger for models with high compactness, ranges from $2.1M_{\odot}$ ($\xi_{2.5,\text{cb}} = 0.20$)² to $2.5M_{\odot}$ (1.15). From Figure 7 in O’Connor & Ott (2011), one can read that the maximum gravitational mass for models with $\xi_{2.5,\text{cb}} = 0.4$ (corresponding to the highest ξ in our solar-metallicity model series) is $\sim 2.2M_{\odot}$, which is bigger than that of the most massive PNS in our solar metallicity 101 models ($M_{\text{PNS}} = 2.16M_{\odot}$ for s23.4 model with $\xi_{2.5} = 0.4273$, see also Figure 14). In their 1D GR study, a model with $\xi_{2.5,\text{cb}} > 0.4$ leads to a BH formation at $t_{\text{pb}} \lesssim 1$ s. For a given BH-forming progenitor model, the BH formation timescale might be delayed in our 2D exploding models because the shock expansion would possibly make the

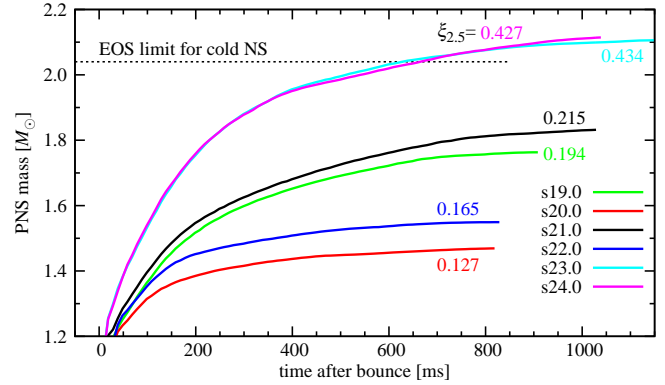


Fig. 9. Time evolution of central PNS mass for the same models as in Figure 8. The compactness parameter $\xi_{2.5}$ is labelled beside each line. The horizontal dotted line represents the maximum mass of a cold neutron star of the LS220 EOS.

mass accretion onto the PNS smaller. Although multi-D GR simulations with elaborate neutrino transport scheme are needed to unambiguously clarify this issue, above exploratory discussions lead us to speculate that the BH formation is less likely to affect the systematic features obtained in our solar metallicity models. We will comment further on the possible effects of the BH formation in section 5 including metal-deficient progenitors.

Regarding the diagnostic energy of the explosion (Fig.10), it is still increasing at $t = t_{\text{fin}}$ and its converged value is difficult to be inferred from our simulations. The time when the diagnostic energy turns upward corresponds to the time of shock revival (t_{400}). We define its increasing rate as $\dot{E}_{\text{dia}} \equiv E_{\text{dia}}(t = t_{\text{fin}})/(t_{\text{fin}} - t_{400})$ in units of 10^{51} erg s⁻¹ and find that it tends to become higher for models with high compactness (0.754, 1.12, and 1.44, for s22.0, s23.0 and s24.0, respectively). This also indicates that the diagnostic energy of the high- ξ models would become higher later on. Note that in previous 1D studies with simplified neutrino heating and cooling scheme (O’Connor & Ott 2011) or with the excision inside the PNS (Ugliano et al. 2012), the relation between the compactness and these explosion properties could not be determined in a self-consistent manner.

We investigate the postbounce shock evolution in more details for three specific models, s11.2, s15.0, and s27.0. The density profile of model s11.2 falls rapidly off with radius and the compactness parameter $\xi_{2.0} = 0.014$ is one of the smallest values among the 101 progenitors, whereas models s15.0 and s27.0 have relatively high compactness ($\xi_{2.0} = 0.298$ and 0.326) casting more extended envelope out to the iron core (see Figure 1 for s15.0 model). Color-coded panels in Figure 11 show the different post-bounce evolutions for s11.2 (left), s15.0 (middle) and s27.0 (right). Model s11.2 explodes rather early ($t_{400} = 150$ ms) and convective activity as well as the oscillations of the shock is moderate before the onset of the explosion (see the bottom left panel). Note in the bottom panels that the anisotropic velocity v_{aniso} (*upper*), and the

¹ Following Suwa et al. (2010) and Nakamura et al. (2014), we define the *diagnostic* energy that refers to the integral of the energy over all outward moving zones that have a positive sum of the specific internal, kinetic, and gravitational energy.

² Note that in O’Connor & Ott (2011) the compactness parameter is estimated at the bounce time ($\xi_{M,\text{cb}}$) using LS180 EOS.

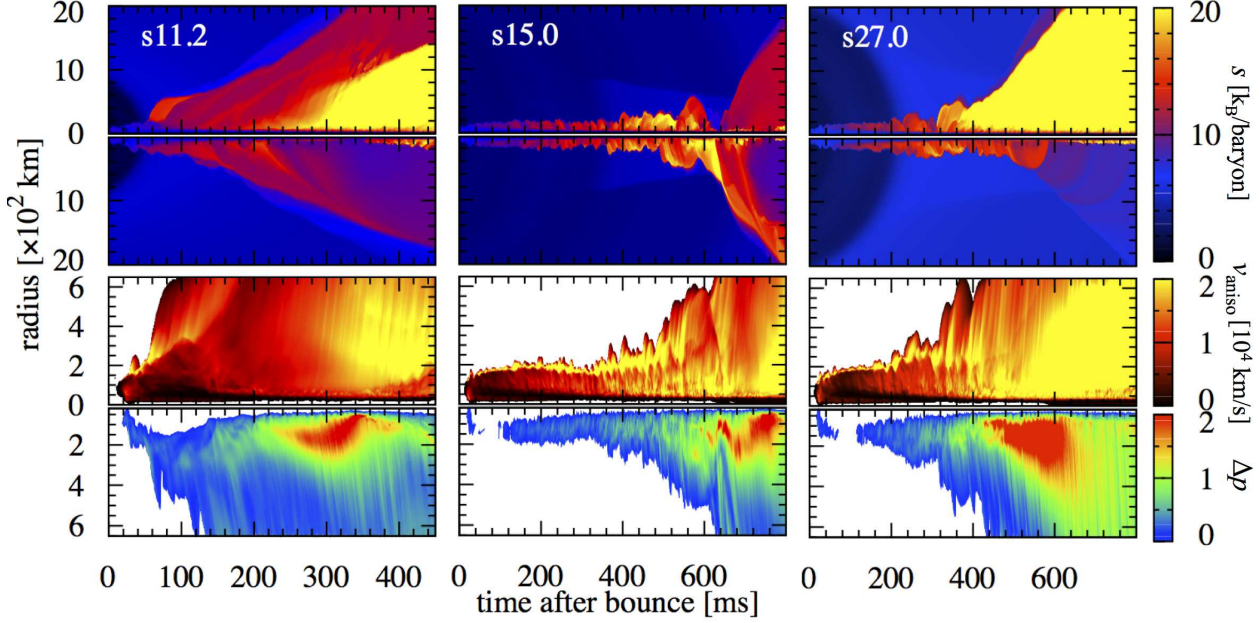


Fig. 11. Time-space diagrams of specific entropy (k_B/baryon , k_B is the Boltzmann constant), anisotropic velocity (cm/s), and pressure perturbation for models s11.2 (left), s15.0 (middle), and s27.0 (right). Top: the specific entropy along the north (upper panels) and south pole (lower). Bottom: time evolution of the anisotropic velocity v_{aniso} (upper) and the normalized pressure perturbation Δp (lower) in the post-shock region (see the text for details).

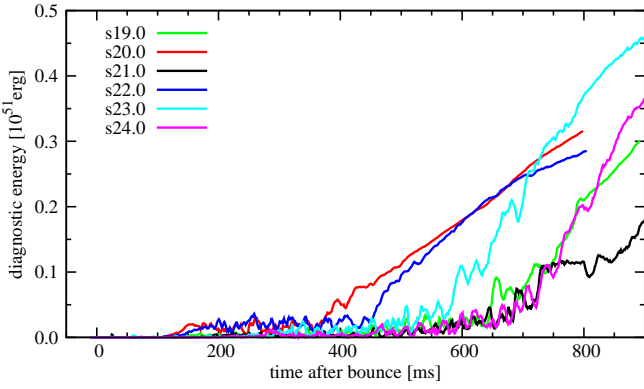


Fig. 10. Same as Figure 9 but of the diagnostic energy of the explosion.

normalized pressure perturbation Δp (lower), is defined respectively as $v_{\text{aniso}} = \sqrt{\langle \rho [(v_r - \langle v_r \rangle)^2 + v_\theta^2] \rangle / \langle \rho \rangle}$ and $\Delta p = \sqrt{\langle p^2 \rangle - \langle p \rangle^2} / \langle p \rangle$, where $\langle A \rangle$ represents the angle average of quantity A (e.g., Takiwaki et al. 2012; Kuroda et al. 2012).

For model s15.0 with higher compactness parameter, sloshing motions of the shock are more clearly visible (middle panels of Figure 11). These features regarding the dominance of the SASI over neutrino-driven convection for high- ξ models are quantitatively consistent with those observed in previous 2D simulations with more detailed neutrino transport scheme (e.g., Müller et al. 2012a). The accreting flows receive an abrupt deceleration near at the

bottom of the gain region, below which the regions are convectively stable. A strong pressure perturbation forms there (seen, in the lower part of the bottom-middle panel in Figure 11, as a boundary between the regions colored by white and deep blue at a radius of $r \lesssim 100$ km after $t_{\text{pb}} \sim 100$ ms). In the so-called advective acoustic cycle (e.g., Foglizzo et al. (2015) for a review), the pressure perturbations subsequently propagate outward before they hit the shock. This leads to the formation of the next vortices (e.g., yellow regions behind the shock in the v_{aniso} plot). These features, as previously identified, are natural outcomes of the SASI and neutrino-driven convection (e.g., Fernández et al. 2014 and references therein). When the residency timescale becomes enough long compared to the neutrino-heating timescale in the gain region due to these multi-D effects, the runaway shock expansion initiates at $t_{\text{pb}} \sim 500$ ms ($t_{400} = 556$ ms) for this model.

Here we emphasize that the use of the leakage scheme, together with the omission of inelastic neutrino scattering on electrons is likely to facilitate artificially easier explosions (Takiwaki et al. 2014). Another caveat is GR effects that cannot be treated in our Newtonian simulations. Discrepancies between our Newtonian models and GR models might become remarkable especially for progenitors with high compactness because our simulations show that the high-compactness models leave more massive PNSs. Comparing model s27.0 ($\xi_{2.5} = 0.232$) for example, the GR model in Müller et al. (2012a) presents more rapid revival of the shock ($t_{400} \sim 205$ ms) than our Newtonian model ($t_{400} = 432$ ms). According to Müller et al. (2012b), GR models lead to higher luminosities and

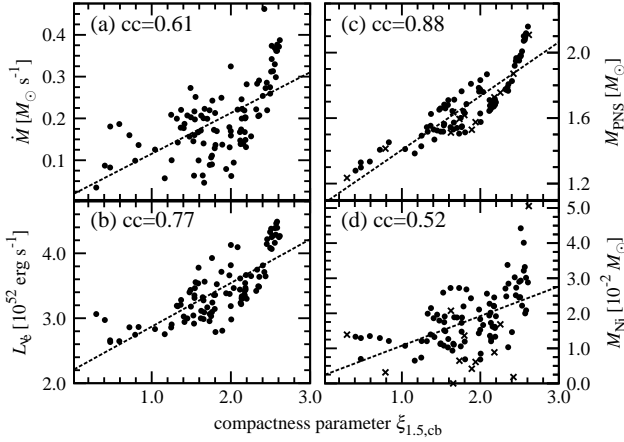


Fig. 12. Resultant supernova properties from our 101 simulations as a function of the compactness parameter $\xi_{1.5,cb}$. Left: (a) Mass accretion rate \dot{M} , and (b) electron neutrino luminosity $L_{\nu e}$, estimated at time of shock revival t_{400} . Right: (c) mass of PNS M_{PNS} , and (d) mass of nickel M_{Ni} in outgoing unbound material, at final time of our simulations t_{fin} . Dashed lines present linear fitting with correlation coefficient denoted in each panel. In the right panels, failed models which cannot carry the shock to the outer boundary during our simulation time are shown by cross and excluded when we estimate the correlation coefficient.

mean energies of neutrinos and therefore to larger heating efficiencies in the gain layer, which is favorable to an explosion. For models with the moderate compactness parameters, we like to note that some key hydrodynamic features in the postbounce phase (such as the onset time of shock revival t_{400}) are rather similar between ours versus the Garching models based on Hanke et al. (2013) ($t_{400} = 640$ vs. 580 ms for model s18.4 ($\xi_{2.5}=0.188$), 320 vs. 400 ms for s19.6 (0.119), 540 vs. 560 ms for s21.6 (0.181), 460 vs. 460 ms for s22.4 (0.200), respectively, e.g., Janka et al., TAUP Conference, 2013).

4. CCSN Properties and Compactness

In Figures 12 - 14, we plot various quantities to summarize the 101 solar-metallicity models as a function of the three different choices of the compactness parameters (Fig.12 ($\xi_{1.5,cb}$), Fig.13 ($\xi_{2.0}$), and Fig.14 ($\xi_{2.5}$)). In each figure, the left panels show the mass accretion rate \dot{M} and electron-type neutrino luminosity $L_{\nu e}$ estimated at radius $r = 500$ km at time $t = t_{400}$. Two panels in the right columns show the PNS mass M_{PNS} and the mass of nickel in the ejected material M_{Ni} at the final simulation time $t = t_{fin}$. Each quantity is fitted by a linear line and each panel contains a correlation coefficient (cc) defined as

$$cc \equiv \frac{\sum_i (\xi_i - \bar{\xi})(y_i - \bar{y})}{\sqrt{\sum_i (\xi_i - \bar{\xi})^2} \sqrt{\sum_i (y_i - \bar{y})^2}}, \quad (2)$$

where \bar{y} is a arithmetic mean of quantity y_i .

For most of our models (89 models) t_{fin} is defined as

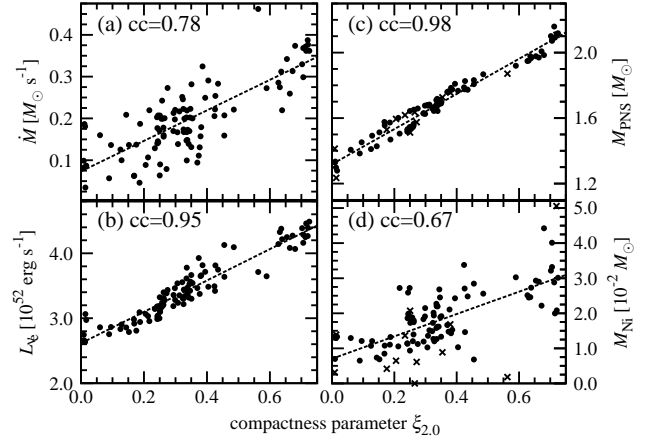


Fig. 13. Same as Figure 12 but as a function of $\xi_{2.0}$.

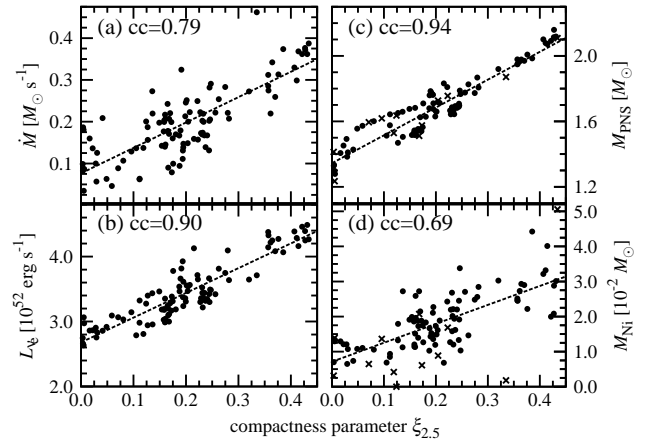


Fig. 14. Same as Figure 12 but as a function of $\xi_{2.5}$.

the time when the maximum shock radius touches the outer boundary. In the remaining 12 models, the shock of model s25.0 has not yet reached the outer boundary within our simulation time ($t_{sim} = 1.5$ s). The other eleven models are stopped during t_{sim} because the density near the outer boundary of the computation domain goes below the lowest value covered by the EOS table. Fortunately, the shock revival occurs in these eleven models before we stopped the simulations, so that we can measure \dot{M} and $L_{\nu e}$ at $t = t_{400}$. These incomplete models are not taken into account when we estimate the correlation coefficients for M_{PNS} and M_{Ni} at $t = t_{fin}$. Note that it is technically challenging to extend the EOS table smoothly to the non-NSE regime where our 13-species alpha network needs to be also consistently treated between the two regimes. We leave this for future work.

Ugliano et al. (2012) were the first to show that various quantities shown in our Figures 12 - 14 are not a mono-

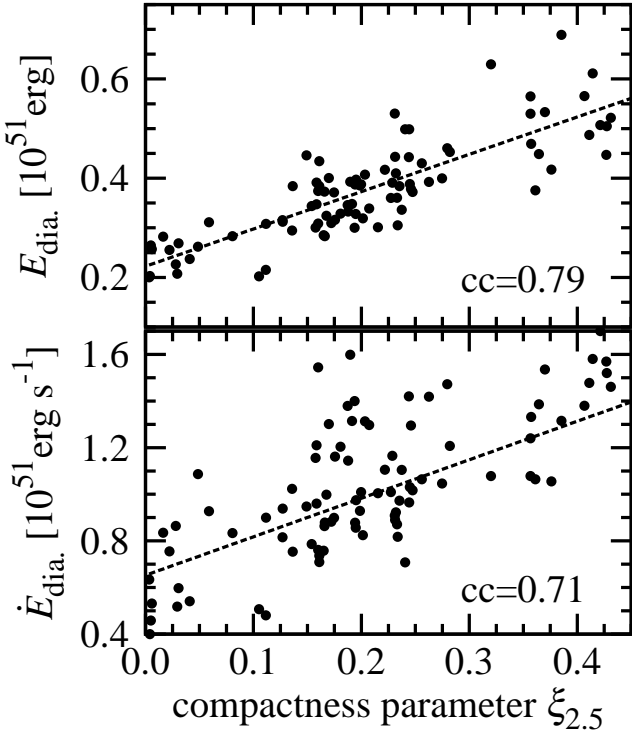


Fig. 15. The diagnostic energy of the explosion at $t = t_{\text{fin}}$ (top panel) and its growth rate (bottom) as a function of $\xi_{2.5}$.

tonic function of the ZAMS mass. We confirm it in our 2D simulations and find that these values are nearly in the linear correlation with the compactness parameters. Furthermore we point out that the correlation becomes higher for the choice of $\xi_{2.0}$ or $\xi_{2.5}$ compared to $\xi_{1.5, \text{cb}}$. This can be interpreted as follows: the core of high- ξ models is surrounded by high-density Si/O layers and the mass accretion rate therefore remains high long after the stalled shock has formed (Figures 13(a) and 8). This makes the PNS mass of the high- ξ models heavier (Figure 13(c)). Due to the high accretion rate, the accretion neutrino luminosities become higher for models with high ξ (Figure 13(b), see also O'Connor & Ott 2013). As a result, we obtain a stronger shock revival powered by the more intense neutrino heating, which makes the amount of the synthesized nickel bigger (Figure 13(d)).

The diagnostic energy of the explosion for the 101 models is in the range between $\sim 0.2 - 0.7 \times 10^{51}$ erg, which is still increasing at the final time of our simulation. (see Figure 10). To obtain a converged value of the diagnostic energy, we need to perform a very long-term simulation including the special care about the smooth transition of the EOS to the non-NSE regime, which is beyond the scope of this work. Instead of the converged value, we estimate the growth rate of the diagnostic energy \dot{E}_{dia} defined in Section 3 and plot it in Figure 15. Both of the diagnostic

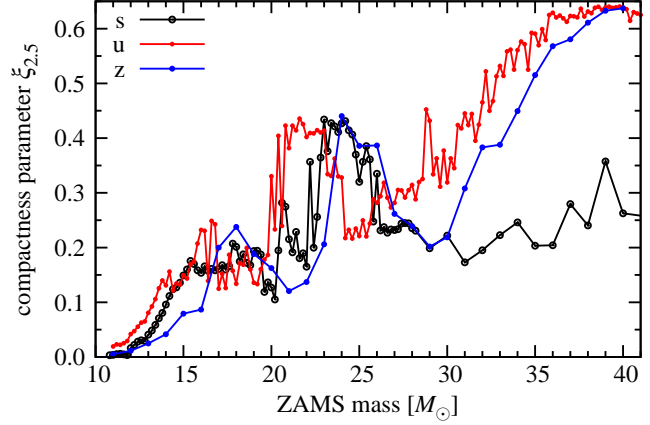


Fig. 16. Compactness parameters $\xi_{2.5}$ of all progenitors as a function of ZAMS mass. Labels s, u, and z, denotes solar- Z_{\odot} , ultra metal-poor $10^{-4} Z_{\odot}$, and zero metallicity, respectively.

energy and its growth rate are moderately correlated with the compactness parameter.

5. Metal-deficient Progenitors

In this section we move on to discuss the results of metal-deficient progenitors. The ultra metal-poor models of $10^{-4} Z_{\odot}$ contains 247 models with the mass increment of $0.2 M_{\odot}$ between 11 and $65 M_{\odot}$ and a $75 M_{\odot}$ model. The masses of the zero-metallicity progenitors are 11 to $40 M_{\odot}$ in every $1.0 M_{\odot}$ (30 models in this series).

Figure 16 compares $\xi_{2.5}$ of these low metallicity models with that of the solar-metallicity models (Figure 2). Since the metal-deficient models experience no mass loss during the stellar evolution, the compactness of the metal-poor stars is shown to be much higher for $\gtrsim 30 M_{\odot}$ than that of the solar-metallicity models.

Figure 17 shows the mass accretion rate \dot{M} (top panel) and the electron-neutrino luminosity $L_{\nu e}$ (bottom) as a function of the compactness parameter $\xi_{2.5}$. These two quantities are estimated at the time of shock revival t_{400} . Regardless of the different initial metallicity, the two quantities show a similar increasing trend. In particular the electron neutrino luminosity is well fitted (the correlation coefficients ≥ 0.90) by a linear line. Some of the ultra metal-poor progenitors with high $\xi_{2.5}$ (> 0.45 , which do not appear in solar-metallicity models) present very high accretion rate and neutrino luminosity above the linear trend.

Figure 18 shows the PNS mass M_{PNS} (top panel) and the mass of the synthesized nickel M_{Ni} in the outgoing unbound material (bottom) as a function of the compactness parameter $\xi_{2.5}$. These two quantities are estimated at final time of our simulations t_{fin} . All of the models again show a similar increasing trend. Crosses in the top panel of Figure 18 represents the models in which the revived shock did not reach the outer boundary during our

simulation time ($t = 1.5$ s)³. We exclude all the unsuccessful (non-exploding) models shown by the crosses in the top panel of Figure 18 when we estimate the correlation coefficients.

The central PNS of the models in the upper-right corner of Figure 18 would finally collapse to form a black hole (BH), although our Newtonian code cannot follow such dynamical behaviors. Triangles in the top right panel of Figure 18 represent the maximum PNS masses estimated by O'Connor & Ott (2011) in which the same progenitor models (Woosley et al. 2002) and the same EOS (LS220) as in this study were examined by their 1D GR code. The dotted curve ($M_{\text{PNS,max}} = 0.52\xi_{2.5} + 2.01$) is a linear fitting to their results. Our models above the dividing line should be predominantly affected by general relativity and such models cannot be treated appropriately by our Newtonian code.

The number fraction of the progenitor models which leave PNS more massive than $M_{\text{PNS,max}}$ is $104/378 \sim 28$ %. Most of them belong to the u-series (98/104), the ZAMS mass of which is bigger than $32.2M_{\odot}$. Adopting the Salpeter initial mass function to weight the ZAMS mass gives $\int_{32.2M_{\odot}}^{75M_{\odot}} m^{-2.35} dm / \int_{10M_{\odot}}^{75M_{\odot}} m^{-2.35} dm \sim 15$ %. Although the majority of the PNSs in our 2D models is less than the maximum mass of PNS, we need to perform GR simulations (e.g., O'Connor & Ott (2011); Müller et al. (2012a); Kuroda et al. (2012)) in order to elucidate the fate of the high- ξ metal-poor stars.

6. Conclusions and Discussion

We have presented an overview of 2D core-collapse supernova simulations employing neutrino transport scheme by the IDSA scheme. We studied 101 solar-metallicity, 247 ultra metal-poor, and 30 zero-metal progenitors covering zero-age main sequence mass from $10.8 M_{\odot}$ to $75.0 M_{\odot}$. Using the 378 progenitors in total, we systematically investigated how the differences in the structures of these multiple progenitors impact the hydrodynamics evolution. By following a long-term evolution over 1.0 s after bounce, most of the computed models exhibited neutrino-driven revival of the stalled bounce shock at $\sim 200 - 800$ ms postbounce, leading to the possibility of explosion. Pushing the boundaries of expectations in previous one-dimensional (1D) studies, our results confirmed that the compactness parameter ξ that characterizes the structure of the progenitors is also a key in 2D to diagnose the properties of neutrino-driven explosions. Models with high ξ undergo high ram pressure from the accreting matter onto the stalled shock, which affects the subsequent evolution of the shock expansion and the mass of the protoneutron star under the influence of neutrino-driven convection and the standing accretion-shock instability. We have shown that the accretion luminosity becomes higher for models with high ξ , which makes the growth rate of diagnostic

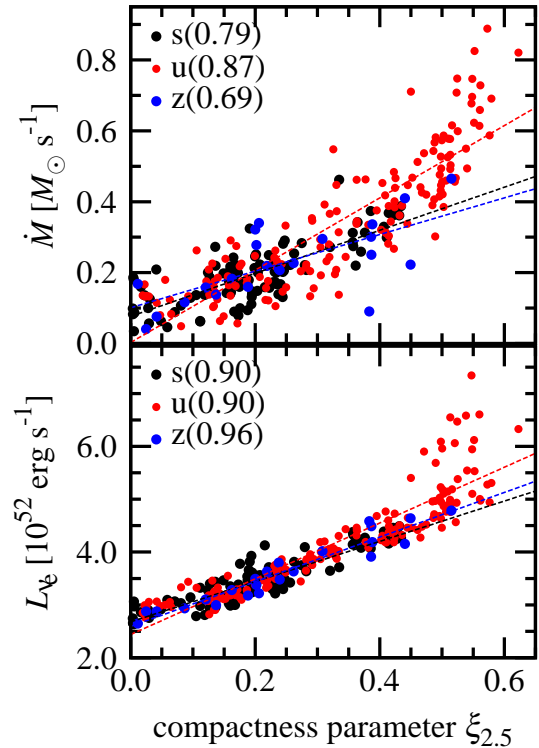


Fig. 17. Mass accretion rate \dot{M} (top panel) and electron neutrino luminosity $L_{\nu e}$ (bottom) as a function of the compactness parameter $\xi_{2.5}$. These two quantities are estimated at time of shock revival t_{400} for all models. Dashed lines present linear fitting with correlation coefficient denoted in each panel for each progenitor type.

energy higher and the synthesized nickel mass bigger. We have found that these explosion characteristics tend to show a monotonic increase as a function of the compactness parameters ξ .

Our simulations are limited in space ($r < 5000$ km) and time ($t \leq 1.5$ s). The simulations are terminated before the diagnostic energies are saturated. Later on neutrino energy deposition would get smaller with time as the neutrino luminosity as well as post-shock density becomes smaller. Further global simulation, taking account of gravitational energy of an envelope and nuclear energy released via recombination process behind the shock, is necessary to determine the final explosion energy (Figure 15). Moreover, the finding of this study should be reexamined by 3D models (Hanke et al. 2012; Dolence et al. 2013; Couch 2013; Couch & O'Connor 2014; Nakamura et al. 2014), in which neutrino transport is appropriately solved (see, discussions in Hanke et al. 2013; Takiwaki et al. 2014; Nagakura et al. 2014; Mezzacappa et al. 2014). It is also important to study the impacts of the precollapse non-spherical structures (e.g., Arnett & Meakin 2011) on fostering the shock revival (e.g., Couch & Ott 2013). To get a more accurate amount of the synthesized nickel and

³ Some of them lying in low $\xi_{2.5}$ ($\lesssim 0.4$) are caused by a numerical reason, that is, as we have already mentioned, our simulations are stopped when a low density region out of our EOS table emerged.

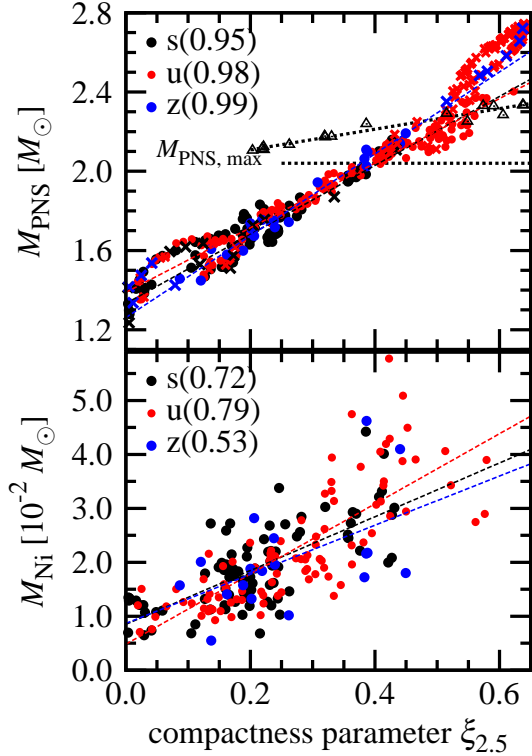


Fig. 18. Mass of PNS (M_{PNS} , top panel) and mass of nickel in outgoing unbound material (M_{Ni} , bottom) as a function of the compactness parameter $\xi_{2.5}$. These two quantities are estimated at final time of our simulations ($t = t_{\text{fin}}$). Failed models which cannot carry the shock to the outer boundary during our simulation time are shown by crosses and excluded when we estimate the correlation coefficient. The horizontal dotted line in the top panel shows the maximum mass of cold NS for LS220 EOS ($2.04 M_{\odot}$). The another dotted line in the top panel is a linear fit of the triangles, the maximum PNS masses of BH forming models in O'Connor & Ott (2011) (see the text for detail).

other isotopes, a post-process calculation with a larger nuclear network is needed. In the more long run, wide-range long-term 3D full-scale GR simulations are needed to unambiguously clarify the critical ξ parameter, below or above which neutron stars or black holes will be left behind.

In this work we have reported our results of only progenitors from one modelling group. Currently we are conducting the same sort of CCSN simulations for sets of progenitors from the other groups including a variety of metallicity, rotation, and magnetic fields, which will be presented in the forthcoming work.

We thank F.K. Thielemann, M. Liebendörfer, R. M. Cabezón, M. Hempel, and K.-C. Pan for stimulating discussions and for their kind hospitality during our research stay at Basel in February, 2014. We are also grateful to S. Yamada and Y. Suwa for informative discussions. Numerical computations were carried out in part on XC30

and general common use computer system at the center for Computational Astrophysics, CfCA, the National Astronomical Observatory of Japan, Oakleaf FX10 at Supercomputing Division in University of Tokyo, and on SR16000 at YITP in Kyoto University. This study was supported in part by the Grants-in-Aid for the Scientific Research from the Ministry of Education, Science and Culture of Japan (Nos. 23540323, 23340069, 24103006, 24244036, and 26707013) and by HPCI Strategic Program of Japanese MEXT.

References

- Arnett, W. D., & Meakin, C. 2011, *ApJ*, 733, 78
- Bethe, H. A. 1990, *Reviews of Modern Physics*, 62, 801
- Blondin, J. M. & Mezzacappa, A. 2007, *Nature*, 445, 58
- Blondin, J. M., Mezzacappa, A., & DeMarino, C. 2003, *ApJ*, 584, 971
- Bruenn, S. W., Mezzacappa, A., Hix, W. R., et al. 2013, *ApJL*, 767, L6
- Bruenn, S. W., Lentz, E. J., Hix, W. R., et al. 2014, *arXiv:1409.5779*
- Buras, R., Rampp, M., Janka, H.-T., & Kifonidis, K. 2006, *A&A*, 447, 1049
- Burrows, A., Hayes, J., & Fryxell, B. A. 1995, *ApJ*, 450, 830
- Burrows, A. 2013, *Reviews of Modern Physics*, 85, 245
- Couch, S. M. 2013, *ApJ*, 775, 35
- Couch, S. M., & Ott, C. D. 2013, *ApJL*, 778, L7
- Couch, S. M., & O'Connor, E. P. 2014, *ApJ*, 785, 123
- Dolence, J. C., Burrows, A., Murphy, J. W., & Nordhaus, J. 2013, *ApJ*, 765, 110
- Dolence, J. C., Burrows, A., & Zhang, W. 2014, *arXiv:1403.6115*
- Einfeldt, B. 1988, *SIAM Journal on Numerical Analysis*, 25, 294
- Fernández, R., Müller, B., Foglizzo, T., & Janka, H.-T. 2014, *MNRAS*, 440, 2763
- Fernández, R. & Thompson, C. 2009, *ApJ*, 697, 1827
- Foglizzo, T., Galletti, P., Scheck, L., & Janka, H.-T. 2007, *ApJ*, 654, 1006
- Foglizzo, T., Scheck, L., & Janka, H.-T. 2006, *ApJ*, 652, 1436
- Foglizzo, T., Masset, F., Guilet, J., & Durand, G. 2012, *Physical Review Letters*, 108, 051130
- Foglizzo, T., Kazeroni, R., Guilet, J., et al. 2015, *arXiv:1501.01334*
- Guilet, J. & Foglizzo, T. 2012, *MNRAS*, 421, 546
- Herant, M., Benz, W., Hix, W. R., Fryer, C. L., & Colgate, S. A. 1994, *ApJ*, 435, 339
- Hanke, F., Marek, A., Müller, B., & Janka, H.-T. 2012, *ApJ*, 755, 138
- Hanke, F., Müller, B., Wongwathanarat, A., Marek, A., & Janka, H.-T. 2013, *ApJ*, 770, 66
- Hayes, J. C., Norman, M. L., Fiedler, R. A., et al. 2006, *ApJS*, 165, 188
- Heger, A., Langer, N., & Woosley, S. E. 2000, *ApJ*, 528, 368
- Heger, A., Woosley, S. E., & Spruit, H. C. 2005, *ApJ*, 626, 350
- Hempel, M., Fischer, T., Schaffner-Bielich, J., & Liebendörfer, M. 2012, *ApJ*, 748, 70
- Iwakami, W., Kotake, K., Ohnishi, N., Yamada, S., & Sawada, K. 2008, *ApJ*, 678, 1207
- . 2009, *ApJ*, 700, 232
- Janka, H.-T., & Mueller, E. 1996, *A&A*, 306, 167
- . 2012, *Annual Review of Nuclear and Particle Science*, 62, 407
- Kitaura, F. S., Janka, H.-T., & Hillebrandt, W. 2006, *A&A*, 450, 345
- Kotake, K., Sumiyoshi, K., Yamada, S., et al. 2012, *Progress of Theoretical and Experimental Physics*, 2012, 01A301
- Kuroda, T., Kotake, K., & Takiwaki, T. 2012, *ApJ*, 755, 11
- Kuroda, T., Takiwaki, T., & Kotake, K. 2015, *arXiv:1501.06330*
- Lattimer, J. M., & Swesty, F. D. 1991, *Nuclear Physics A*, 535, 331
- Liebendörfer, M., Whitehouse, S. C., & Fischer, T. 2009, *ApJ*, 698, 1174
- Limongi, M., & Chieffi, A. 2006, *ApJ*, 647, 483
- Marek, A. & Janka, H.-T. 2009, *Astrophys. J.*, 694, 664
- Müller, E. & Janka, H.-T. 1997, *A&A*, 317, 140
- Müller, B., Janka, H.-T., & Heger, A. 2012a, *ApJ*, 761, 72
- Müller, B., Janka, H.-T., & Marek, A. 2012b, *ApJ*, 756, 84
- Müller, B., Janka, H.-T., & Marek, A. 2013, *ApJ*, 766, 43
- Mueller, B., & Janka, H.-T. 2014, *arXiv:1409.4783*
- Murphy, J. W., & Burrows, A. 2008, *ApJ*, 688, 1159
- Murphy, J. W., Dolence, J. C., & Burrows, A. 2013, *ApJ*, 771, 52
- Mezzacappa, A., Bruenn, S. W., Lentz, E. J., et al. 2014, *arXiv:1405.7075*
- Mezzacappa, A., Bruenn, S. W., Lentz, E. J., et al. 2015, *arXiv:1501.01688*
- Nagakura, H., Sumiyoshi, K., & Yamada, S. 2014, *arXiv:1407.5632*
- Nakamura, K., Takiwaki, T., Kotake, K., & Nishimura, N. 2014, *ApJ*, 782, 91
- Nakamura, K., Kuroda, T., Takiwaki, T., & Kotake, K. 2014, *arXiv:1403.7290*
- Nomoto, K., & Hashimoto, M. 1988, *Phys. Rep.*, 163, 13
- Ohnishi, N., Kotake, K., & Yamada, S. 2006, *ApJ*, 641, 1018
- Ott, C. D., Burrows, A., Dessart, L., & Livne, E. 2008, *ApJ*, 685, 1069
- O'Connor, E., & Ott, C. D. 2011, *ApJ*, 730, 70
- O'Connor, E., & Ott, C. D. 2013, *ApJ*, 762, 126
- Pejcha, O., & Thompson, T. A. 2014, *arXiv:1409.0540*
- Perego, A., Hempel, M., Fröhlich, C., et al. 2015, *arXiv:1501.02845*
- Radice, D., Couch, S. M., & Ott, C. D. 2015, *arXiv:1501.03169*
- Sukhbold, T., & Woosley, S. E. 2014, *ApJ*, 783, 10
- Sumiyoshi, K., Takiwaki, T., Matsufuru, H., & Yamada, S. 2014, *arXiv:1403.4476*
- Suwa, Y., Kotake, K., Takiwaki, T., et al. 2010, *PASJ*, 62, L49
- Suwa, Y., Yamada, S., Takiwaki, T., & Kotake, K. 2014, *arXiv:1406.6414*
- Takiwaki, T., Kotake, K., & Suwa, Y. 2012, *ApJ*, 749, 98
- Takiwaki, T., Kotake, K., & Suwa, Y. 2014, *ApJ*, 786, 83
- Uglio, M., Janka, H.-T., Marek, A., & Arcones, A. 2012, *ApJ*, 757, 69
- Woosley, S. E., & Heger, A. 2007, *Phys. Rep.*, 442, 269
- Woosley, S. E., Heger, A., & Weaver, T. A. 2002, *Reviews of Modern Physics*, 74, 1015
- Woosley, S. E., & Weaver, T. A. 1995, *ApJS*, 101, 181

Appendix 1. Numerical Resolution

Numerical resolution should be taken as high as possible in order to capture accurately hydrodynamics processes in computational fluid dynamics. In the state-of-the-art CCSN simulations, especially in multi-D models, however, high numerical resolution drastically increases the numerical cost and a full convergence has not yet been obtained even in simplified simulations.

Hanke et al. (2012) investigated the resolution dependence in their 2D and 3D models using 11.2 and 15 M_{\odot} progenitors with a parameterized neutrino heating and cooling scheme. In most of the 2D models, better angular resolution led to easier explosion, although some of them do not obey this trend. On the other hand, Couch (2013) investigated a 15 M_{\odot} progenitor employing the same simple neutrino scheme as in Hanke et al. (2012), and found

that 2D explosions are delayed for models with higher numerical resolution. More recently, Takiwaki et al. (2014) computed 2D and 3D models for an $11.2M_{\odot}$ progenitor with an energy-dependent neutrino transport scheme and concluded that higher numerical resolutions led to slower onset of the shock revival in both 2D and 3D.

In our fiducial 2D runs, the angular resolution ($\Delta\theta$) is taken as 1.4° (128 angular zones to cover $0 \leq \theta \leq \pi$). In this Appendix, we briefly discuss the resolution dependence, in which we compare the results with the fiducial resolution with those with high resolution ($\Delta\theta = 0.7^{\circ}$ with 256 angular zones).

Figure 19 shows time evolution of the average shock radii for two progenitors, s11.2 and s15.0. In both of the two, it is shown that the shock revival is delayed for the high-resolution models (thin lines). The difference of t_{400} , t_{1000} , and t_{2500} (the time when the average shock radius arrives at 400, 1,000, and 2,500 km, respectively) are 30.4 % (13.1 %), 29.0 % (2.9 %), and 6.8 % (3.1 %) for model s11.2 (s15.0). The relatively large difference of t_{400} may reflect that the shock revival time is more likely to be affected by stochastic matter motions driven by neutrino-driven convection and the SASI.

The evolution of the diagnostic energies are presented in Figure 20. Comparing them at $t = t_{1000}$ and t_{2500} , the differences between the fiducial and high resolution models are 22.7 % (9.8 %) and 28.9 % (13.9 %) for s11.2 (s15.0) model. The difference is more bigger in model s11.2, which has a small compactness parameter and is weakly exploding, than in model s15.0.

Our fiducial resolution does not give well-converged results at least for model s11.2. The systematic behaviors that we found, as shown in Figure 13 for example, might be subject to change quantitatively. At least, our 2D results showing that higher numerical resolutions lead to slower evolution of the shock radius and the diagnostic explosion energy, are consistent with Couch (2013) and Takiwaki et al. (2014). A systematic resolution study including a detailed comparison between different numerical codes, schemes, and setups should be done urgently, which we leave for future work.

Appendix 2. Time of Shock Revival

Our systematic 2D CCSN simulations demonstrate that the ξ parameter is a good diagnostics to infer the progenitor-remnant and progenitor-explosion connections. However, the time of shock revival (t_{400}) shows a large scatter and weaker correlation with the compactness parameter. Figure 21 shows t_{400} for three kinds of the compactness parameters and we obtain low correlation coefficients (0.45-0.54). This may partly come from the stochasticity of the nonlinear growth of SASI and convection, seeded by initial random perturbations, which affects the subsequent shock evolution. Another possibility is that our definition of the compactness parameters might be inappropriate to characterize t_{400} . In this Appendix, we attempt to find a more appropriate form of the compactness parameter to characterize the shock revival time.

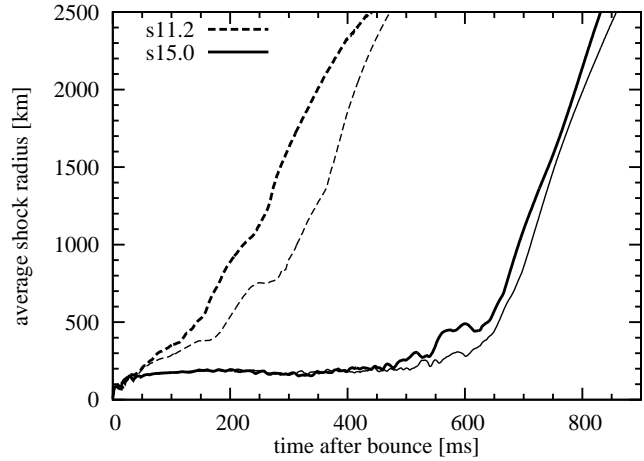


Fig. 19. Comparison between different resolution models. Average shock radii as a function of time relative to bounce for s11.2 and s15.0 models are shown. The shock revives more rapidly in the fiducial resolution models (thick lines) than in high resolution models (thin lines).

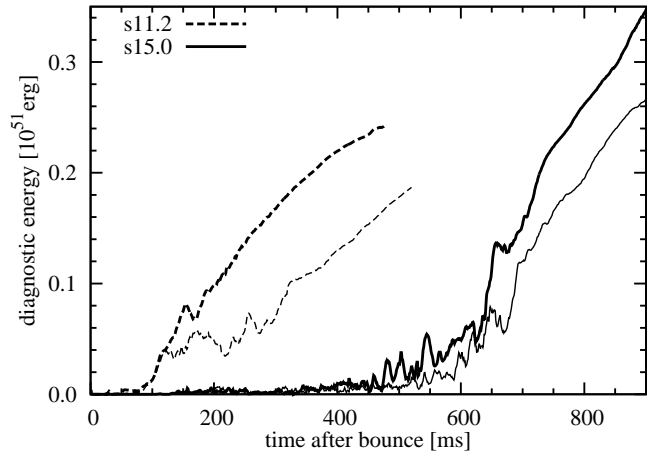


Fig. 20. Same as Figure 19 but for the evolution of the diagnostic energies of the explosion.

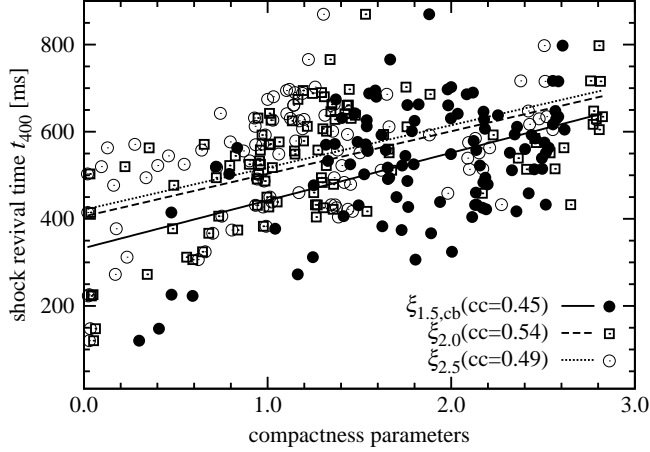


Fig. 21. Time of shock revival t_{400} as three kinds of the compactness parameters. $\xi_{2.0}$ and $\xi_{2.5}$ are calibrated by arbitrary factors.

As we have seen in Figure 8, at least for some models, the shock revival time seems to be linked to the time when the mass accretion rate drops. It typically occurs when the Si/O interface falls onto the shock. To capture this, it would be better to estimate the compactness at the Si/O interface which differs from models to models. In fact, models with earlier shock revival tend to have a more compact Si layer. Here we define another compactness parameter ξ_i as

$$\xi_i \equiv \frac{\Delta M_i / M_\odot}{\Delta R_i / 1000 \text{ km}}, \quad (\text{A1})$$

where subscript i denotes representative element at a certain layer, ΔR_i and ΔM_i corresponds to the width and included mass in the layer, respectively.

Figure 22 presents t_{400} as a function of the ratio $\xi_{\text{Si+Si/O}}/\xi_{\text{Fe}}$. The concept of this alternative parameter is as follows. The compactness parameter defined at the surface of iron core (ξ_{Fe}) is a measure to predominantly determine the core neutrino luminosity, whereas $\xi_{\text{Si+Si/O}}$ is a measure to the density decline in the outer layer. So we expect that the smaller ratio would lead to an easier explodability. As shown in Figure 22, this alternative indicator gives the correlation coefficient of 0.66, which is better than 0.49 estimated from $\xi_{2.5}$. To enhance the predictive power, we should more carefully analyze how the compactness parameters are related to the core/accretion luminosity, and the density jump at Si/O interface. We leave this for the future work.

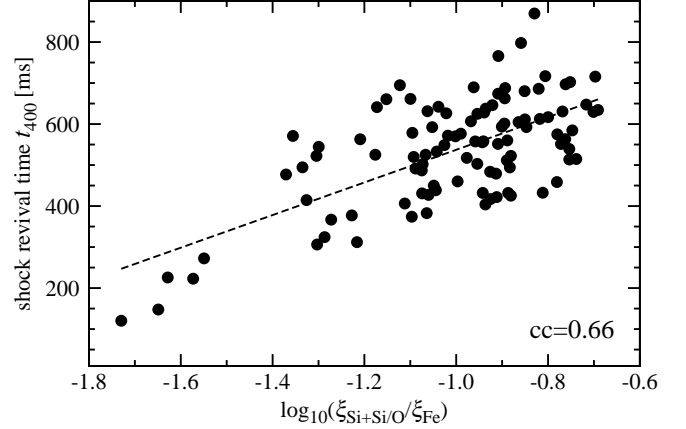


Fig. 22. Time of shock revival t_{400} estimated as a function of the alternative compactness parameter (e.g., Eq. (A1)).